

Measurement of $\gamma p \rightarrow K^+ \Lambda$ and $\gamma p \rightarrow K^+ \Sigma^0$ at photon energies up to 2.6 GeV^{*}

K.-H. Glander^{1,a}, J. Barth¹, W. Braun^{1,3}, J. Hannappel^{1,3}, N. Jöpen¹, F. Klein¹, E. Klempt², R. Lawall¹, J. Link^{2,3}, D. Menze¹, W. Neuberger^{1,3}, M. Ostrick¹, E. Paul¹, I. Schulday¹, W. J. Schuille¹, H. v. Pee^{2,3}, F. W. Wieland¹, J. Wißkirchen^{1,3}, and C. Wu¹

¹ Physikalisches Institut, Bonn University, Bonn, Germany

² Helmholtz-Institut für Strahlen- und Kernphysik, Bonn University, Bonn, Germany

³ No longer working at this experiment

the date of receipt and acceptance should be inserted later

Abstract. The reactions $\gamma p \rightarrow K^+ \Lambda$ and $\gamma p \rightarrow K^+ \Sigma^0$ were measured in the energy range from threshold up to a photon energy of 2.6 GeV. The data were taken with the SAPHIR detector at the electron stretcher facility, ELSA. Results on cross sections and hyperon polarizations are presented as a function of kaon production angle and photon energy. The total cross section for Λ production rises steeply with energy close to threshold, whereas the Σ^0 cross section rises slowly to a maximum at about $E_\gamma = 1.45$ GeV. Cross sections together with their angular decompositions into Legendre polynomials suggest contributions from resonance production for both reactions. In general, the induced polarization of Λ has negative values in the kaon forward direction and positive values in the backward direction. The magnitude varies with energy. The polarization of Σ^0 follows a similar angular and energy dependence as that of Λ , but with opposite sign.

PACS. 13.60.Le Meson production

1 Introduction

The production of open strangeness in photon-induced hadronic processes on protons provides a tool to investigate the dynamical role of flavours, since a strange quark-antiquark pair is created. This study contributes to the search for missing non-strange resonances which decay into strange particle pairs (see e.g. [2,3]).

We report on measurements of total and differential cross sections and hyperon polarizations in the reaction channels $\gamma p \rightarrow K^+ \Lambda$ ($\Lambda \rightarrow p \pi^-$) and $\gamma p \rightarrow K^+ \Sigma^0$ ($\Sigma^0 \rightarrow \Lambda \gamma$; $\Lambda \rightarrow p \pi^-$) between threshold and a photon energy of 2.6 GeV.

The data were taken with the magnetic multiparticle detector, SAPHIR [4], at the 3.5 GeV electron stretcher accelerator, ELSA [5], with electron beam energies of 2.8 GeV and 2.6 GeV.

Results from SAPHIR on the reactions $\gamma p \rightarrow K^+ \Lambda$ and $\gamma p \rightarrow K^+ \Sigma^0$, based on 30 million triggers taken in 1992-94 with photon energies up to 2.0 GeV, were already published [6].

The new results reported here come from four data taking

^{*} This work is supported in part by the Deutsche Forschungsgemeinschaft (DFG) (SPP 1034 KL 980/2-3)

^a Part of doctoral thesis [1]

Correspondence to: klein@physik.uni-bonn.de

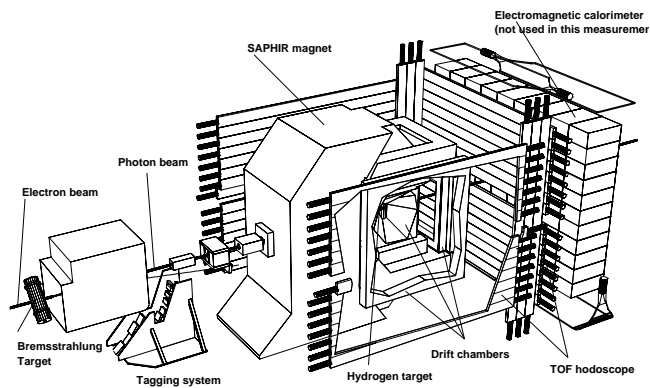


Fig. 1. Sketch of the SAPHIR detector.

periods in 1997/98 where 180 million triggers were collected with tagged photons in an extended energy range up to 2.65 GeV.

The data are available via the internet¹.

2 Experiment and event reconstruction

The magnetic multiparticle detector, SAPHIR [4], is shown schematically in Fig. 1. The extracted electron beam was

¹ <http://saphir.physik.uni-bonn.de/saphir/publications.html>

directed on a radiator target to provide a photon beam which was energy-tagged over the range from about 0.85 GeV to 2.65 GeV (0.8 GeV to 2.45 GeV for electrons of 2.6 GeV). The data taking was based on a trigger defined by a coincidence of signals from the scattered electron in the tagging system with at least two charged particles in the scintillator hodoscopes of SAPHIR and no signal from a beam veto counter of non-interacting photons.

The SAPHIR detector was upgraded for this data taking. A new tagging system with a larger photon energy range [7,8] was installed. The tagging system and the photon beam veto counter were used to measure the photon flux. The tagging system comprises 14 scintillation counters for triggering and time definition and 2 multi-wire proportional chambers defining 703 energy channels. Each scintillation counter is connected to a scaler. Approximately every 0.4 seconds a minimum bias trigger defined by an electron that hits a counter in the tagging system starts a full read-out of the SAPHIR data including the scalers. This event sample was used to calculate a normalisation factor, based on N_e as the number of hits in all tagging scintillators and N_{γ_i} as the number of coincidences between the photon veto counter, the energy channel i , and the associated tagging scintillator. Multiplying the ratio N_{γ_i}/N_e with the total number of hits in the tagging scintillators for a run period provides the photon flux for the channel i . Thus, since data taking and flux normalisation take place simultaneously, any inefficiency of the tagger, even if it varies during the data acquisition, is automatically taken into account.

A planar drift chamber with the same hexagonal drift cell structure as the central drift chamber has been added downstream of the central drift chamber in order to improve the track reconstruction in forward direction [1]. The drift chambers were filled with a gas mixture of neon (63.75%), helium (21.25%) and isobutane (15%). By including the hits of the forward drift chamber in the track fit the momentum resolution for tracks crossing the forward drift chamber was improved on average by a factor of five [1]. The momentum resolution $\Delta p/p$ for a 300 MeV/c particle measured in the central drift chamber is about 2.5%. The forward drift chamber ameliorates the momentum resolution to about 1%. For 1 GeV/c particles $\Delta p/p$ is 7.5% in the central drift chamber and 1.5% with assistance of the forward drift chamber [1].

Events were reconstructed from measurements of the incident photon in the tagging system and charged particles in the drift chamber system.

3 Data selection

The event samples were selected by a sequence of cuts. In a first step events with one track of a negatively charged and two tracks of positively charged particles were selected. Then the reconstruction of a secondary vertex was required, which could be a candidate for a $\Lambda \rightarrow p\pi^-$ decay, and the three-momentum of the Λ candidates was reconstructed and combined with the remaining positive

track considered as a K^+ candidate for the reconstruction of the vertex of the primary γp interaction.

In the next step of selection it was required that an event passes a complete kinematic fit for the hypothesis $\gamma p \rightarrow K^+ \Lambda$ or $\gamma p \rightarrow K^+ \Sigma^0$ at the primary vertex with $\Lambda \rightarrow p\pi^-$ at the secondary vertex and, in case of Σ^0 , also with $\Sigma^0 \rightarrow \Lambda\gamma$ as additional constraint. If an event fitted both hypotheses, the reaction with the higher probability in the kinematic fit was accepted.

For events which passed the fit procedure the missing mass was calculated from the four-momenta (built up with the measured three-momenta combined with mass assignments) of the particles at the primary vertex according to

$$m_{\gamma p - K^+} = \sqrt{(p_\gamma^{in} + p_p^{in} - p_{K^+}^{out})^2} .$$

The distribution of the missing mass is shown in Fig. 2. Clear signals are seen for Λ and Σ^0 as well as indications of excited hyperons on top of background events.

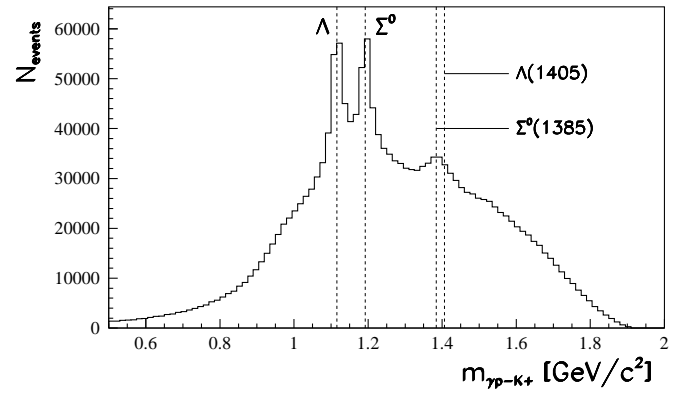


Fig. 2. Distribution of the missing mass $m_{\gamma p - K^+}$ after the selection based on the event topology.

The background was reduced by a sequence of cleaning cuts:

- The events were required to have a primary vertex inside the sensitive target volume (within resolution limits).
- The missing mass $m_{\gamma p - K^+}$ was required to be in the range $1000 \text{ MeV} < m_{\gamma p - K^+} < 1240 \text{ MeV}$ for events selected as $\gamma p \rightarrow K^+ \Lambda$ and $1050 \text{ MeV} < m_{\gamma p - K^+} < 1350 \text{ MeV}$ for events selected as $\gamma p \rightarrow K^+ \Sigma^0$.
- The invariant mass, reconstructed from the four-momenta of the proton and pion at the secondary vertex (before the kinematic fit) according to

$$m_\Lambda = \sqrt{(p_{\pi^-}^{out} + p_p^{out})^2} ,$$

had to be consistent with the nominal Λ mass within the range of $\pm 8 \text{ MeV}$.

- The probability of the kinematic fits had to be greater than 10^{-10} .

After these cleaning cuts the data samples contained 51977 events selected as $\gamma p \rightarrow K^+ \Lambda$ and 54388 events selected

as $\gamma p \rightarrow K^+ \Sigma^0$. The missing mass distributions of both event samples are shown in Fig.3. The migration of events from one reaction to the other has been estimated by means of Monte-Carlo simulated events and the cross sections were corrected correspondingly (see Section 6).

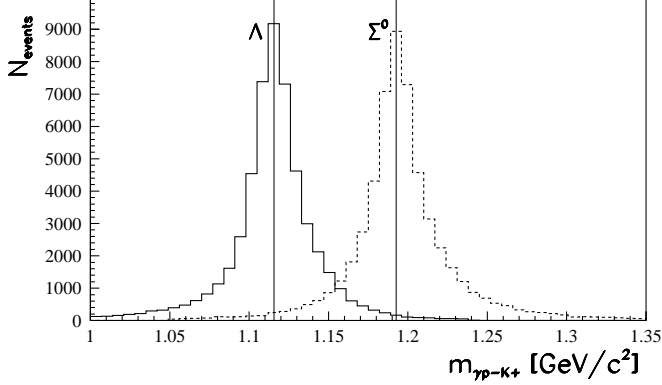


Fig. 3. Distribution of the missing mass $m_{\gamma p - K^+}$ for events from the reactions $\gamma p \rightarrow K^+ \Lambda$ and $\gamma p \rightarrow K^+ \Sigma^0$ after all selection cuts.

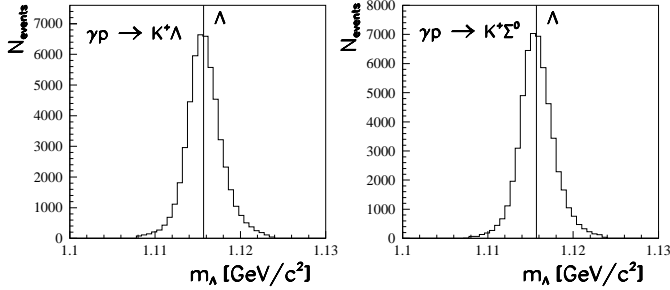


Fig. 4. Distribution of the invariant mass m_{Λ} for the events selected as $\gamma p \rightarrow K^+ \Lambda$ and $\gamma p \rightarrow K^+ \Sigma^0$ respectively. The vertical lines mark the nominal position of the Λ mass.

Fig 4 shows the distribution of the invariant mass m_{Λ} after the selection cuts. The resolution of the reconstructed Λ mass is about 2 MeV.

The reconstructed Λ decay time distributions of both data sets ($K^+ \Lambda, K^+ \Sigma^0$) are shown in Figures 5 and 6. The solid line describes a fit to an exponential function $f(t) = a \cdot e^{-t/\tau_{\Lambda}}$ carried out in the time-range of constant acceptance without using the first time bin. The parameter a was determined in the fits, while τ_{Λ} has been fixed to the PDG lifetime value [9]. The decay time distributions are well described by the fits for both reactions (the values of χ^2 per degrees of freedom, ndf , are given in the figures). Possible background from other reactions which have two positively charged and one negatively charged particles in the final state, such as $\gamma p \rightarrow p \pi^+ \pi^-$ and $\gamma p \rightarrow p \pi^+ \pi^- \pi^0$ ($\gamma p \rightarrow n \pi^+ \pi^- \pi^+$ is suppressed by the kinematic fit), are expected to contribute mainly at small decay times. A corresponding excess of events is not visible. Instead, a loss of events is observed in the first t bin ($0 < t < 10^{-10}$ s), which is due to a migration effect caused by the limited resolution of the reconstructed

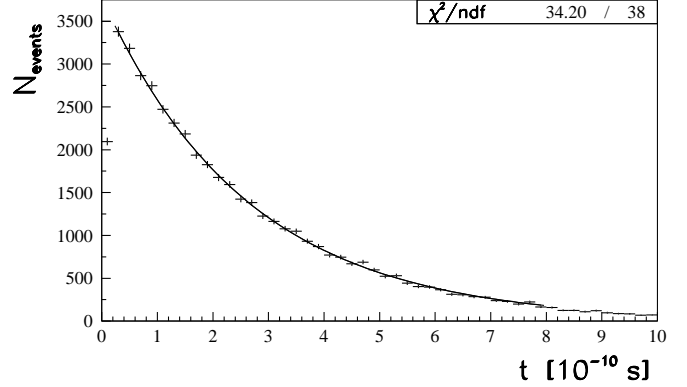


Fig. 5. Distribution of the reconstructed Λ decay time for measured events associated with the reaction $\gamma p \rightarrow K^+ \Lambda$. The solid line is explained in the text.

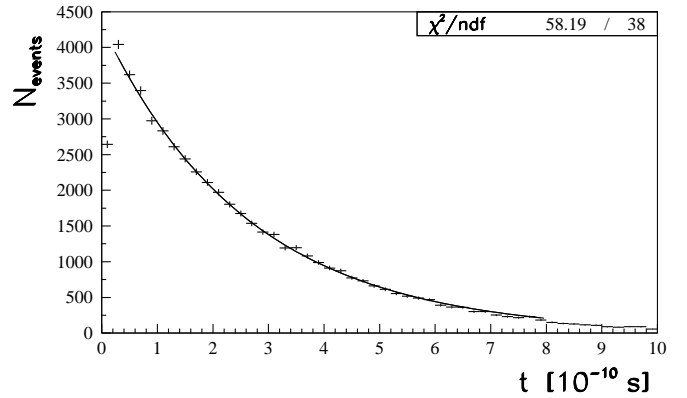


Fig. 6. Distribution of the reconstructed Λ decay time for measured events associated with the reaction $\gamma p \rightarrow K^+ \Sigma^0$. The solid line is explained in the text.

positions of primary and secondary vertices, which was verified with Monte-Carlo simulated events [1].

4 Acceptance corrections

The acceptance of events, which were measured in the SAPHIR setup and had passed reconstruction and selection, was calculated using a simulation package which was developed for SAPHIR based on GEANT 2.0 [10].

The simulation of the response of the detector components comprised the photon tagging system [11,12,8], the scintillator hodoscopes [13,8] and the drift chamber system [1]. The efficiencies of the tagging system and scintillator hodoscopes, which together with the beam veto counter defined the trigger efficiency of the data taking, were determined separately from the data of the four data taking periods and included in the simulations.

The simulation of the drift chamber system was carried out at a very detailed level [1]. In particular, the statistical distribution of the ionization deposits along a track of a charged particle in a drift cell were taken into account so that the drift length of the electron cluster, which is closest to the signal wires, can be longer than the distance of closest approach of the track to the signal wire (see

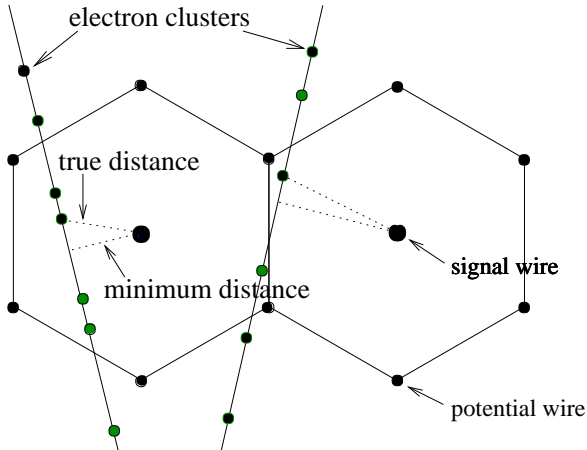


Fig. 7. Two particles, passing the hexagonal drift cells of a planar drift chamber, ionising drift chamber gas molecules as germs for the production of electron clusters along the particle tracks.

Fig. 7). With the gas mixture used for the chambers (see Section 2) this effect was important. While the mean free path length between two ionization deposits, for a particle velocity $\beta \approx 0.5$, is of the order of $200 \mu\text{m}$, which corresponds to the spatial resolution of the chambers², for $\beta \approx 0.9$ it increases up to 2 mm [1].

Drift times simulated at this level describe measured distributions well. This is demonstrated for the final state $p\pi^+\pi^-$ and two β values in Figs. 8 and 9. If the ionization cloud, which determines the drift time, is displaced from the point of closest approach, the actually measured drift time is delayed and the drift distance calculated from the drift time appears prolonged with respect to the minimum distance. Because the mean free path length grows with β one observes on average a shift of drift times to higher values with increasing β values (see Figs. 8 and 9). This is most obvious when looking at the rise of both spectra, which is steeper for low β , and the broadening of the maximum with β .

The spread of the ionization clouds along the track according to the free path length in the chamber gas also affected the reconstruction of the tracks, because hits with significantly prolonged drift distances disturb the track fit calculations directly. That means: In case that the difference between the true and the minimum distance (see Fig. 7) is much larger than the drift chamber resolution, such hits give large contributions to the χ^2 value of the track fit, because in the track reconstruction it has to be assumed that drift times are related to the point of closest approach. Such disturbing hits were removed after the first track fit iteration: If the determined drift distance differed by more than three times the maximal spatial resolution of $300 \mu\text{m}$ from the distance between the fitted track and the signal wire after the first fit, then the hit was rejected. This procedure removed also hits with other problems in the track reconstruction like wrongly resolved left-right

² The spatial resolution is a function of β and changes between $150 \mu\text{m}$ and $300 \mu\text{m}$ [1].

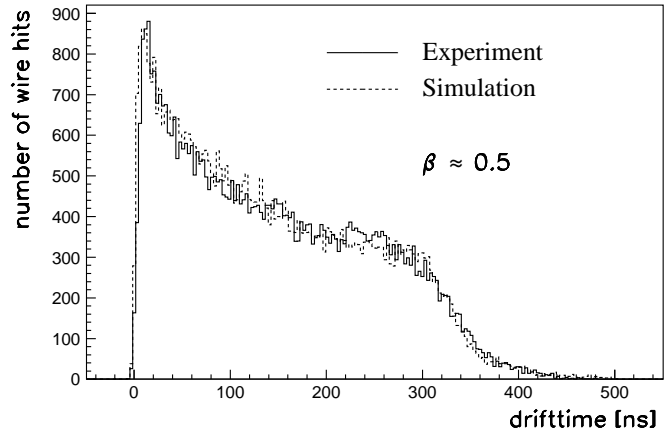


Fig. 8. Drift time spectrum for drift times produced by particles in experimental and simulated events of reaction $\gamma p \rightarrow p\pi^+\pi^-$ with velocities $\beta \approx 0.5$.

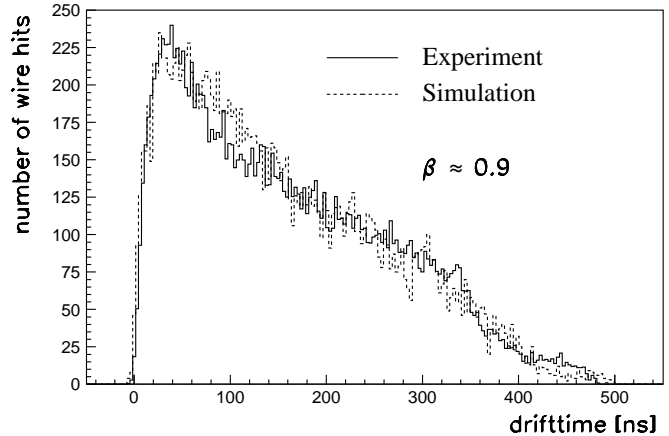


Fig. 9. Drift time spectrum for drift times produced by particles in experimental and simulated events of reaction $\gamma p \rightarrow p\pi^+\pi^-$ with velocities $\beta \approx 0.9$.

ambiguities between tracks and signal wires, to give just an example.

The final track fit was carried out with the remaining hits in the central drift chamber (14 detection layers) and in the forward chamber (12 layers). The distribution of the number of hits used for the final track fit is well described by simulated events. This is shown in Fig. 10, again for $\beta \approx 0.5$ and $\beta \approx 0.9$.

The acceptance was calculated from simulated events as the ratio of finally accepted to generated events in bins of photon energy and kaon production angle in the *cms*. The acceptance values for both reactions, $\gamma p \rightarrow K^+ \Lambda$ and $\gamma p \rightarrow K^+ \Sigma^0$, are of the order of 10% and do nowhere vanish throughout the full kinematic range.

The same simulation package was used for other reactions measured at SAPHIR [8, 11, 15, 16]. The cross sections are in general consistent with existing world data in normalization as well as in energy dependence. As an example, Fig. 11 shows this agreement for the reaction cross section of $\gamma p \rightarrow p\pi^+\pi^-$ which has been measured at SAPHIR with high statistics [8]. This verifies that the acceptance calculations are well understood.

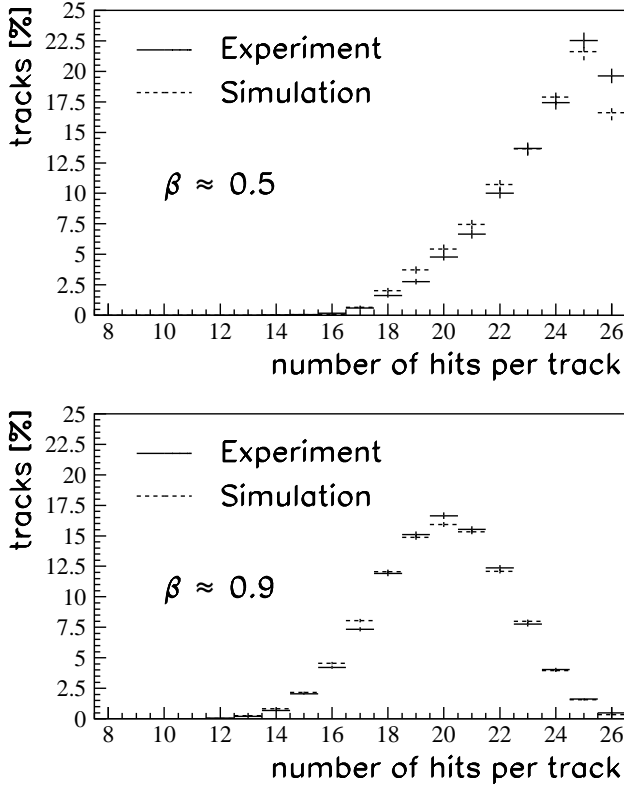


Fig. 10. Number of hits per track after removing bad hits from the track fit.

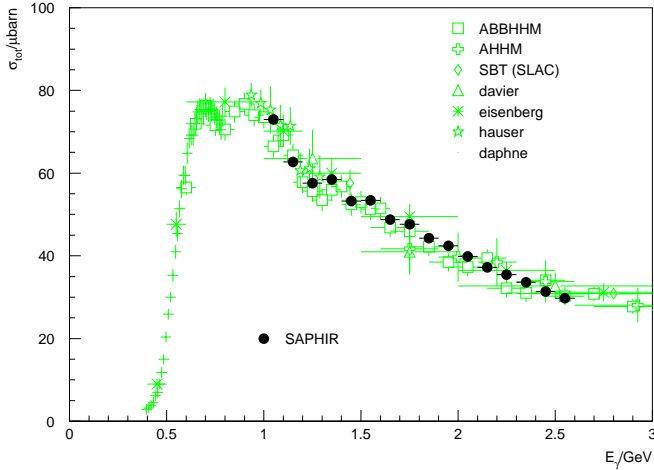


Fig. 11. The total cross section for the reaction $\gamma p \rightarrow p \pi^+ \pi^-$ measured by SAPHIR [8] in comparison with existing world data [14].

5 Cross sections

Cross sections x_i and their uncertainties σ_i ($i = 1, \dots, N$ where N is the number of data taking periods; N is equal 4 or 3 respectively³) were determined as a function of photon energy and K^+ production angle in the overall cms

³ Three of the four data taking periods were carried out with an energy of the primary electron beam of $E_0 = 2.8$ GeV. During one run an electron beam with an energy of $E_0 = 2.6$ GeV was used instead. Therefore, for the determination of

separately for the data taking periods during the years 1997/98. The statistically weighted mean m of the four (three) measurements x_i and its statistical error σ_w were determined according to

$$m = \frac{\sum_{i=1}^N \frac{x_i}{\sigma_i^2}}{\sum_{i=1}^N \frac{1}{\sigma_i^2}}, \quad \sigma_w = \frac{1}{\sqrt{\sum_{i=1}^N \frac{1}{\sigma_i^2}}}.$$

The results on differential cross sections as a function of the K^+ production angle in the overall cms in bins of photon energy are shown for $\gamma p \rightarrow K^+ \Lambda$ in Figures 12, 13 and 14 and for $\gamma p \rightarrow K^+ \Sigma^0$ in Figures 15, 16 and 17, and the numbers are given in Appendix A. The data points in Figures 12 to 17 are the determined weighted means m . The solid bars represent the statistical errors σ_w .

These errors, σ_w , are based on the full statistics of the event samples, but cannot account for systematic uncertainties caused by differences in the run conditions. Known differences were taken into account in the simulation used for acceptance corrections. In order to take into account possible additional fluctuations and uncertainties between the runs, which were not explicitly considered in the simulations, another error σ_d has been calculated which is the standard deviation of the four measurements x_i to the weighted mean m given by the square root of the variance V_m :

$$\sigma_d = \sqrt{V_m} = \sqrt{\frac{1}{N(N-1)} \sum_{i=1}^N (m - x_i)^2}.$$

The dashed bars in Figures 12 to 17 show the errors σ_d obtained for the $N = 4$ runs. In general σ_d is bigger than σ_w . In cases where σ_d was smaller than σ_w , σ_d was set equal to σ_w . σ_w and σ_d were determined as a function of photon energy and kaon production angle. The error defined by $\sqrt{\sigma_d^2 - \sigma_w^2}$ is a measure of the systematic uncertainties due to fluctuations in the run conditions.

The solid lines in the Figs. 12-17 describe fits with Legendre polynomials of the form

$$\frac{d\sigma}{d\cos(\theta_{K^+}^{cms})} = \frac{q}{k} \left(\sum_{l=0}^{L=4} a_l P_l(\cos \theta_{K^+}^{cms}) \right)^2.$$

The phase space factor q/k is given by the ratio of kaon to photon momentum in the overall cms .

The fitted coefficients a_l of the Legendre polynomials are shown as a function of photon energy in Figures 18 and 19. The coefficients show clear structures indicating rapid changes of the production mechanisms.

It is worth to mention that the energy dependence of the coefficients a_0 , a_1 and a_2 in Figures 18 and 19 depends only weakly on the choice of the maximum angular momentum, L , and good χ^2 values for the Legendre fits were obtained for L -values between 2 and 4. For $L = 4$ the mean of all χ^2 values is 0.8 and 90% of all fits the differential cross sections the data of this run were not used for photon energies, E_γ , above 2.4 GeV.

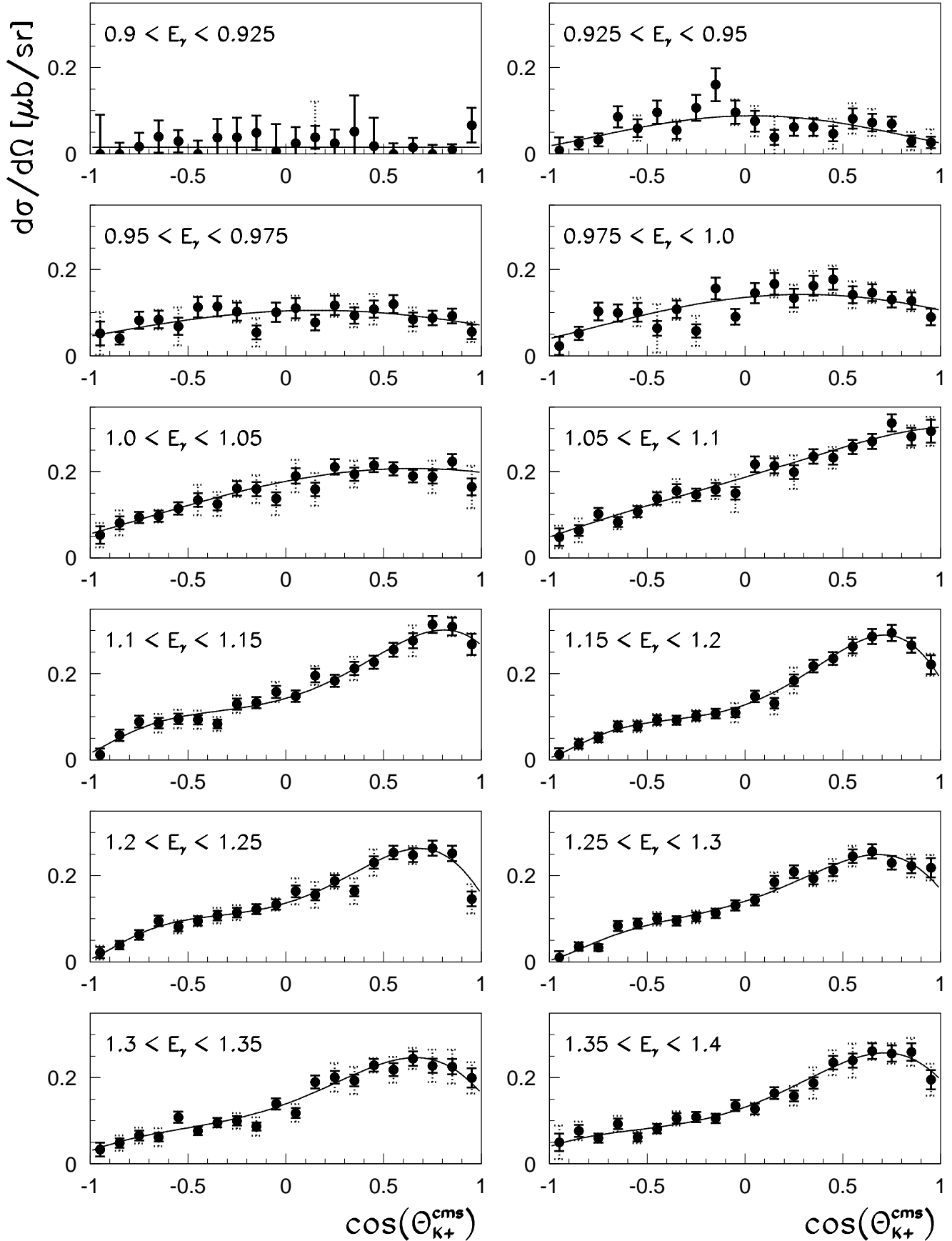


Fig. 12. Differential cross sections of $\gamma p \rightarrow K^+ \Lambda$ for photon energies $0.9 \text{ GeV} < E_\gamma < 1.4 \text{ GeV}$. The solid and dashed bars represent errors σ_w and σ_d (see text). The solid lines describe fits of Legendre polynomials to the data.

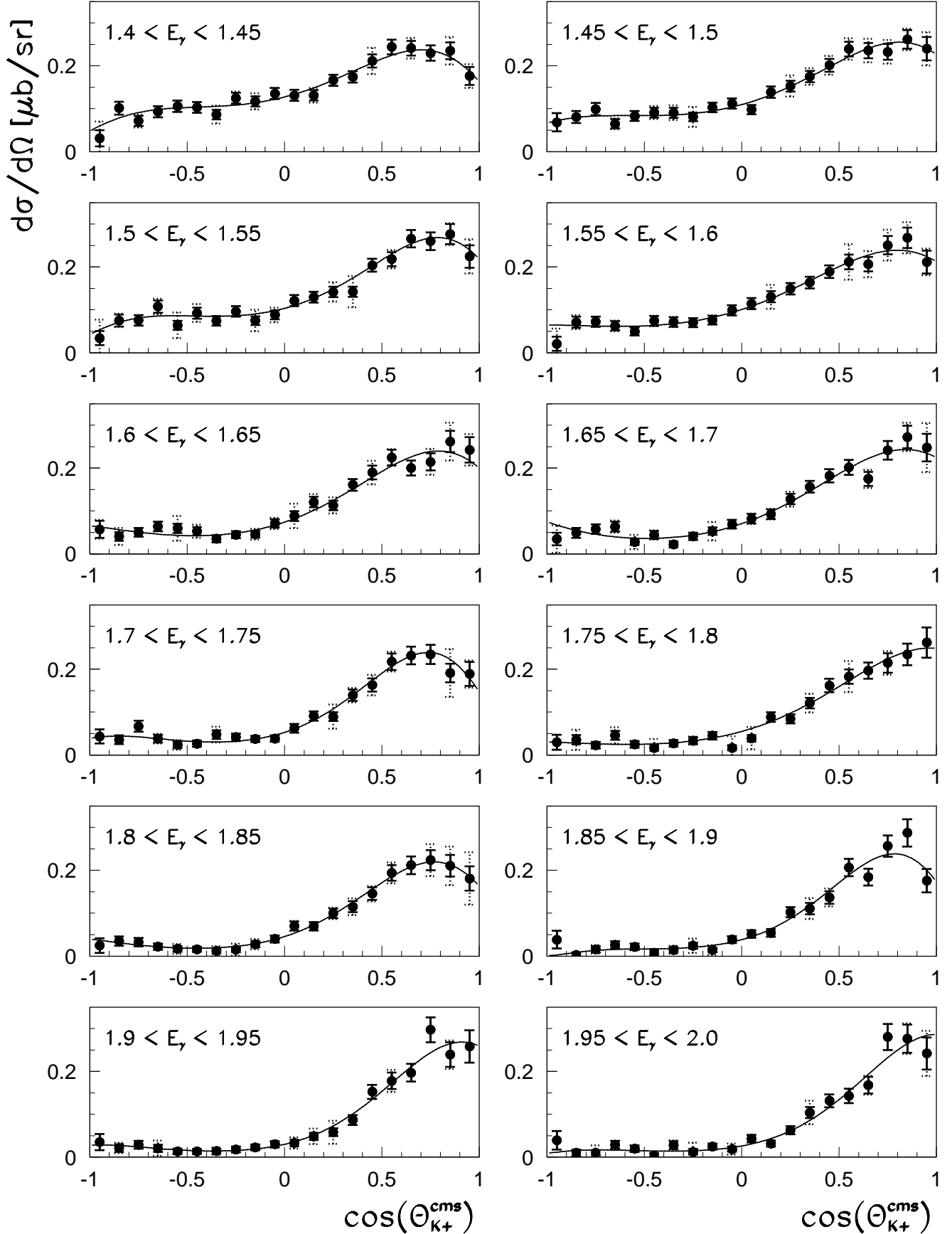


Fig. 13. Differential cross sections of $\gamma p \rightarrow K^+ \Lambda$ for photon energies $1.4 \text{ GeV} < E_\gamma < 2.0 \text{ GeV}$. The solid and dashed bars represent errors σ_w and σ_d (see text). The solid lines describe fits of Legendre polynomials to the data.

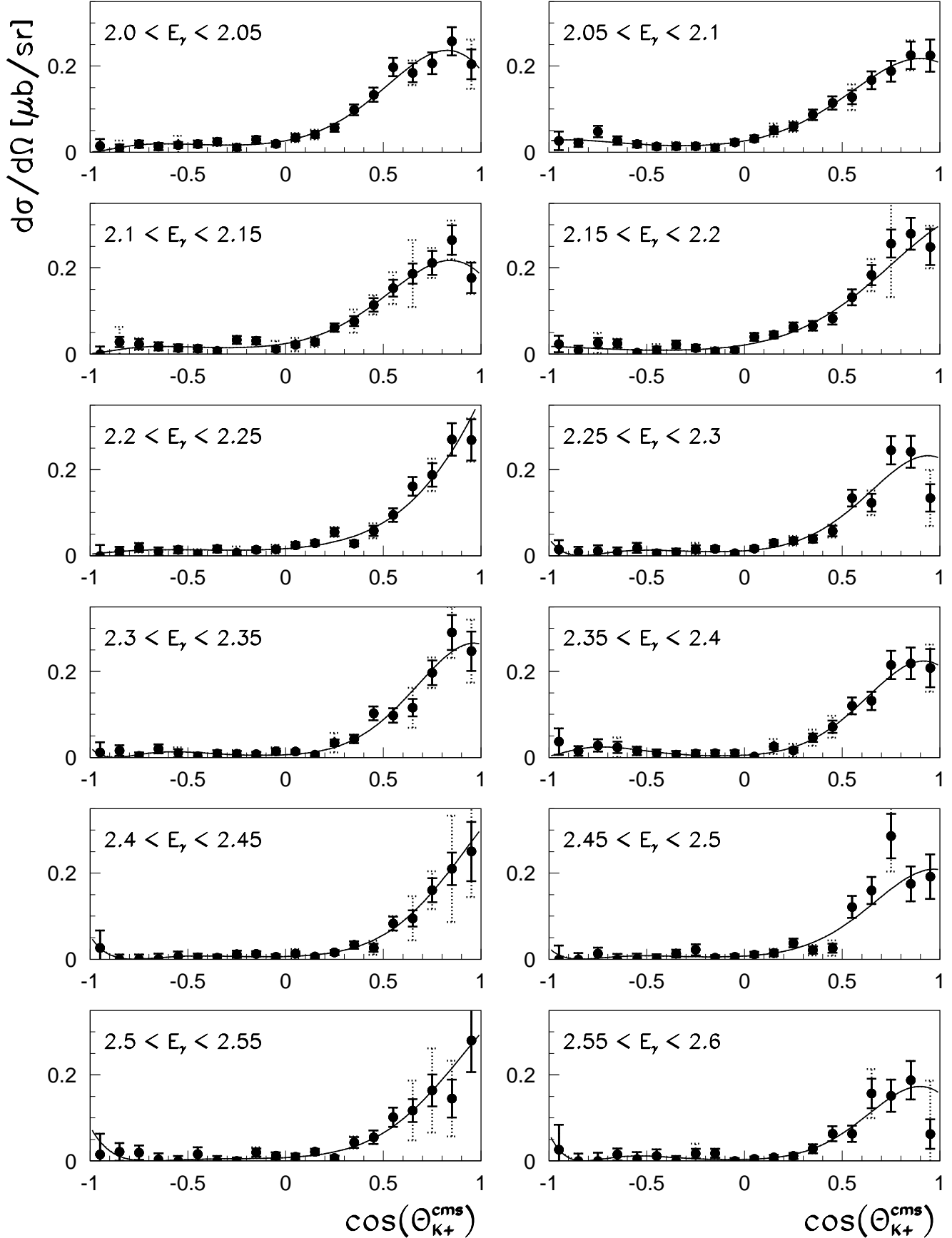


Fig. 14. Differential cross sections of $\gamma p \rightarrow K^+ \Lambda$ for photon energies $2.0 \text{ GeV} < E_\gamma < 2.6 \text{ GeV}$. The solid and dashed bars represent errors σ_w and σ_d (see text). The solid lines describe fits of Legendre polynomials to the data.

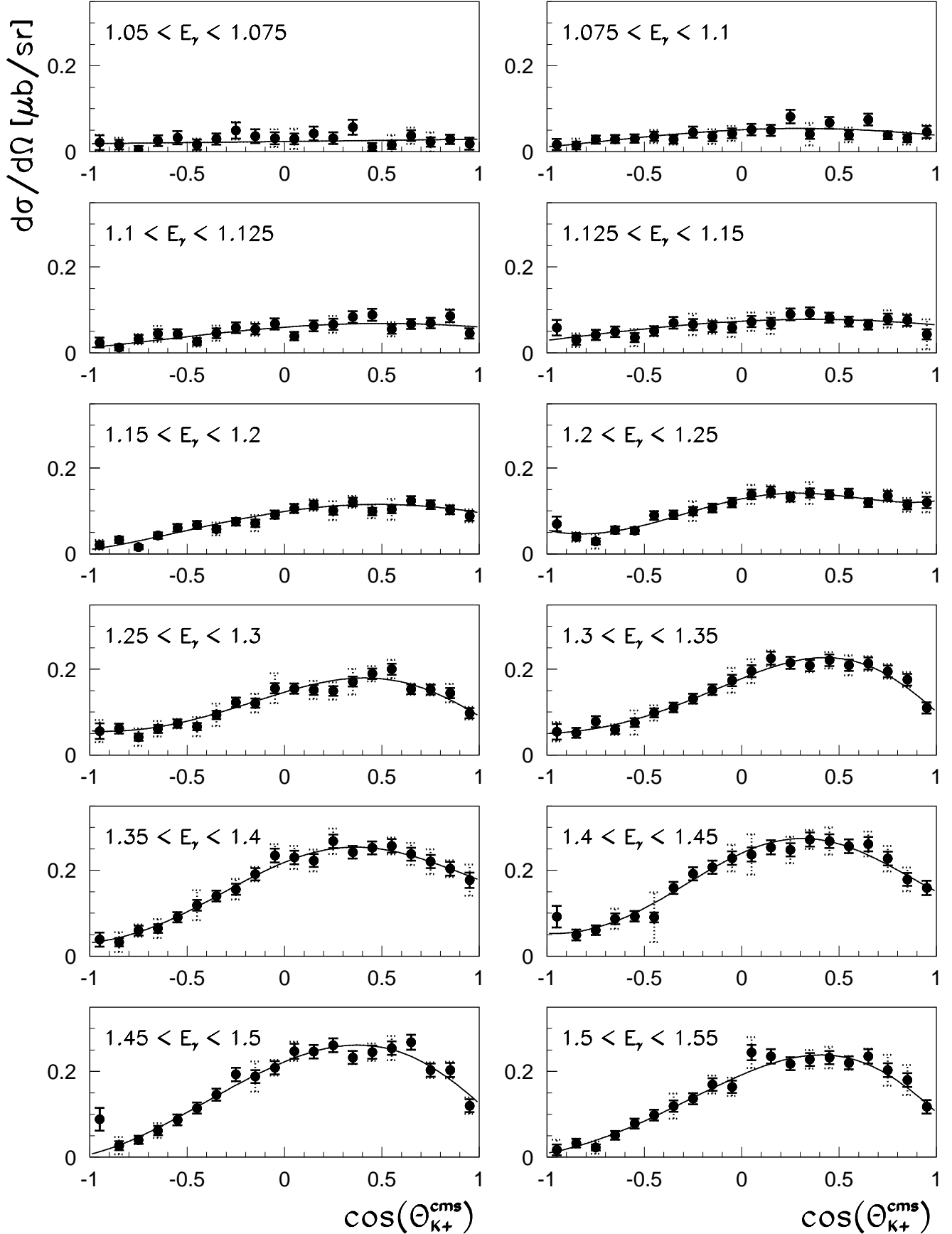


Fig. 15. Differential cross sections of $\gamma p \rightarrow K^+ \Sigma^0$ for photon energies $1.05 \text{ GeV} < E_\gamma < 1.55 \text{ GeV}$. The solid and dashed bars represent errors σ_w and σ_d (see text). The solid lines describe fits of Legendre polynomials to the data.

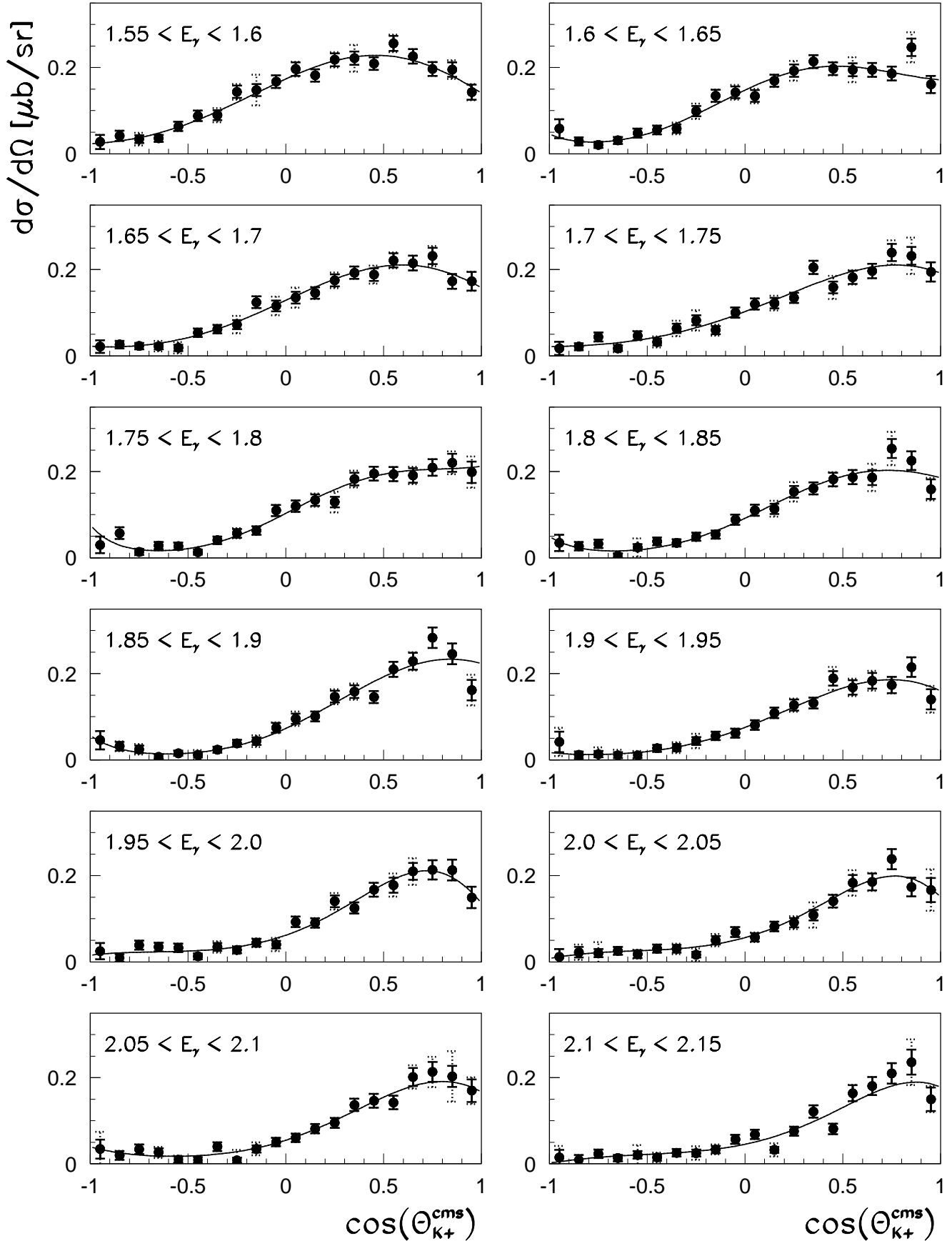


Fig. 16. Differential cross sections of $\gamma p \rightarrow K^+ \Sigma^0$ for photon energies $1.55 \text{ GeV} < E_\gamma < 2.15 \text{ GeV}$. The solid and dashed bars represent errors σ_w and σ_d (see text). The solid lines describe fits of Legendre polynomials to the data.

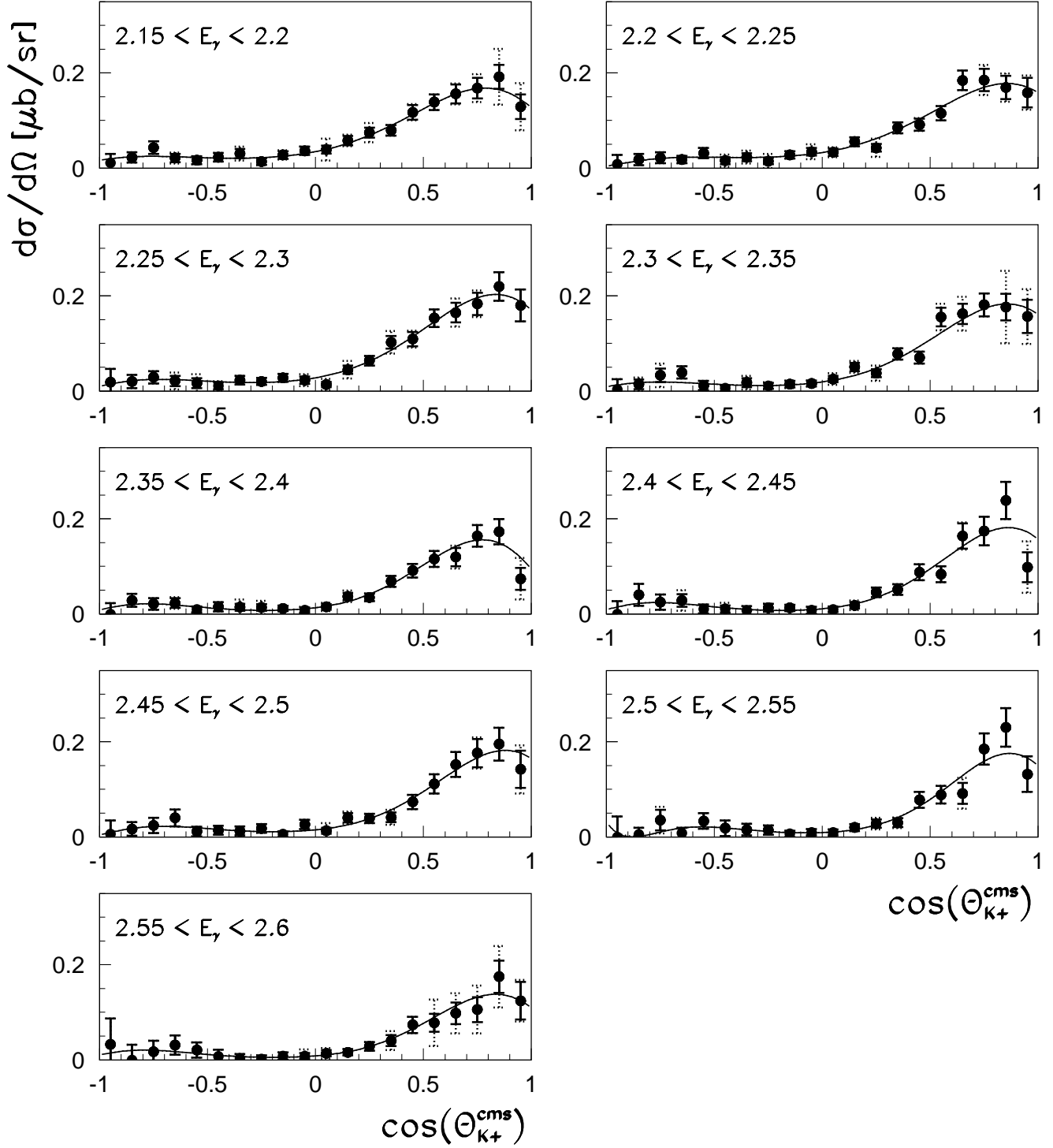


Fig. 17. Differential cross sections of $\gamma p \rightarrow K^+ \Sigma^0$ for photon energies $2.15 \text{ GeV} < E_\gamma < 2.6 \text{ GeV}$. The solid and dashed bars represent errors σ_w and σ_d (see text). The solid lines describe fits of Legendre polynomials to the data.

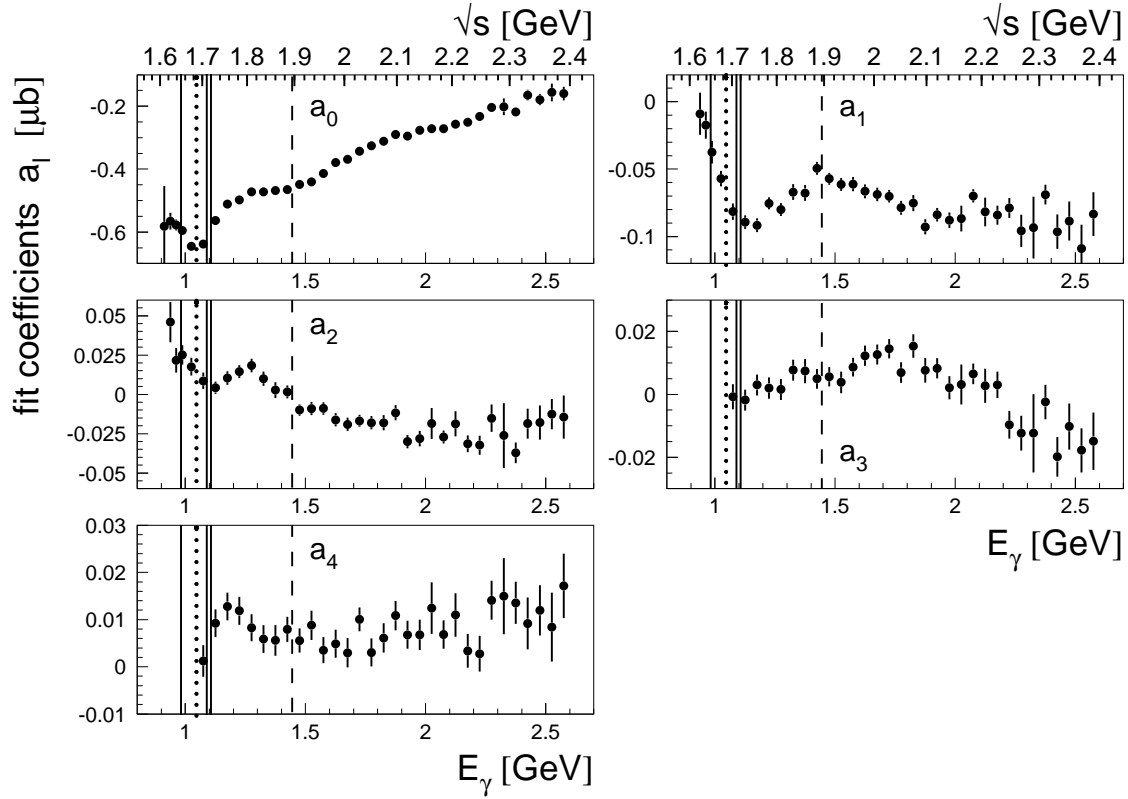


Fig. 18. Legendre polynomial fit coefficients from differential cross sections for the reaction $\gamma p \rightarrow K^+ \Lambda$ as a function of the photon energy. For explanation of the vertical lines see caption of Fig. 20.

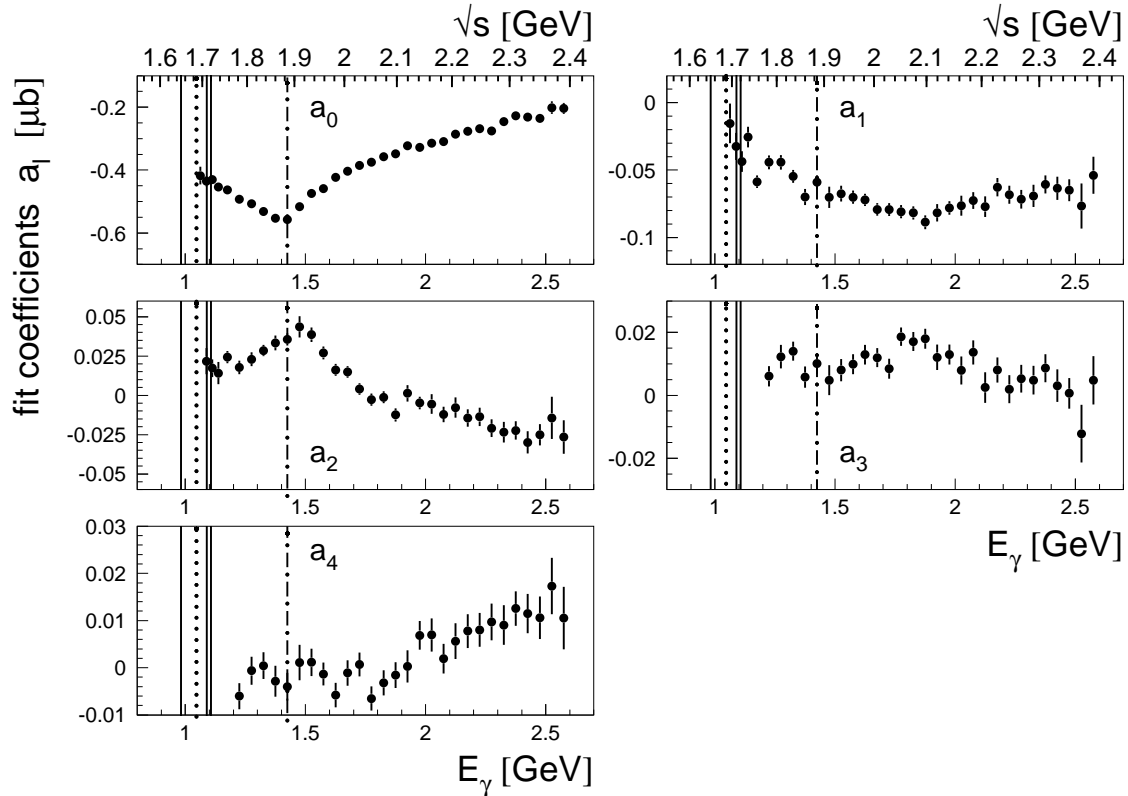


Fig. 19. Legendre polynomial fit coefficients from differential cross sections for the reaction $\gamma p \rightarrow K^+ \Sigma^0$ as a function of the photon energy. For explanation of the vertical lines see caption of Fig. 21.

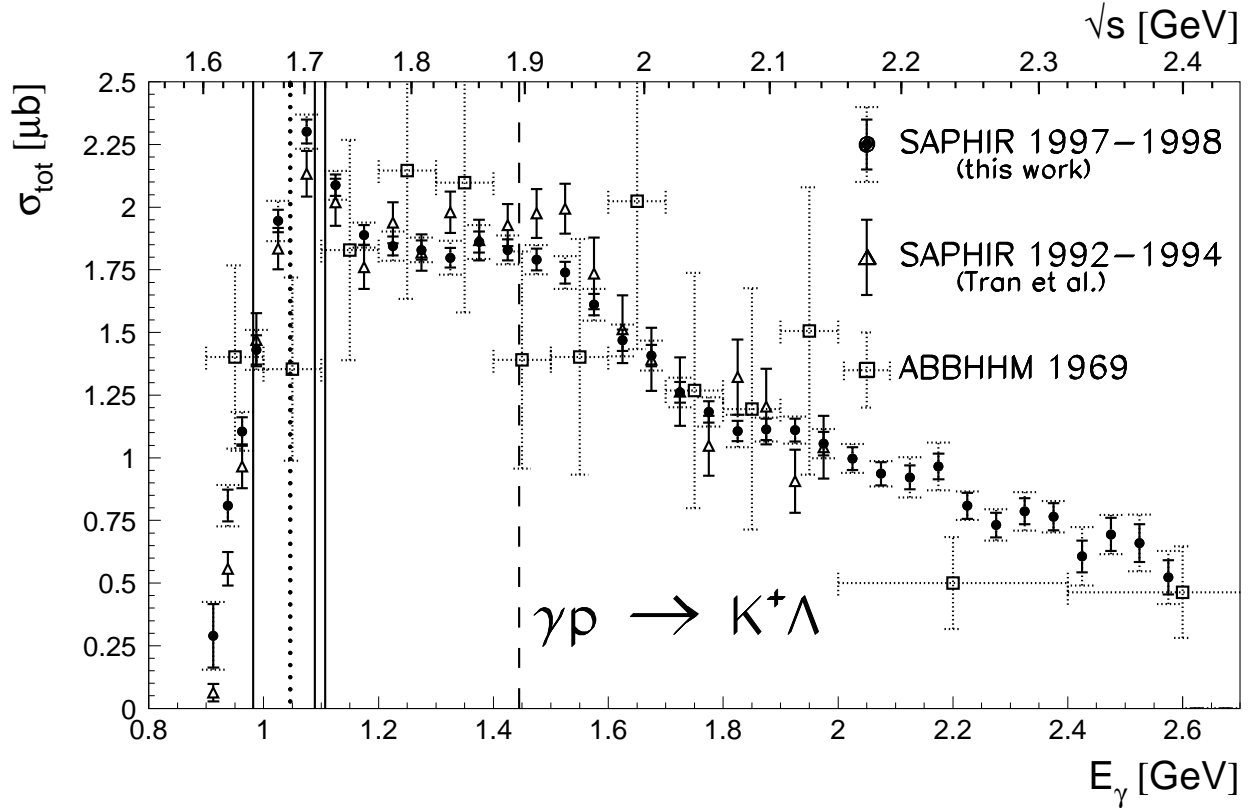


Fig. 20. Total cross section of $\gamma p \rightarrow K^+ \Lambda$. The vertical lines indicate the threshold energy of $\gamma p \rightarrow K^+ \Sigma^0$ (dotted), mass values of the known resonances $S_{11}(1650)$, $P_{11}(1710)$ and $P_{13}(1720)$ (solid) and the position of the hypothetical resonance $D_{13}(1895)$ (dashed) discussed in the text.

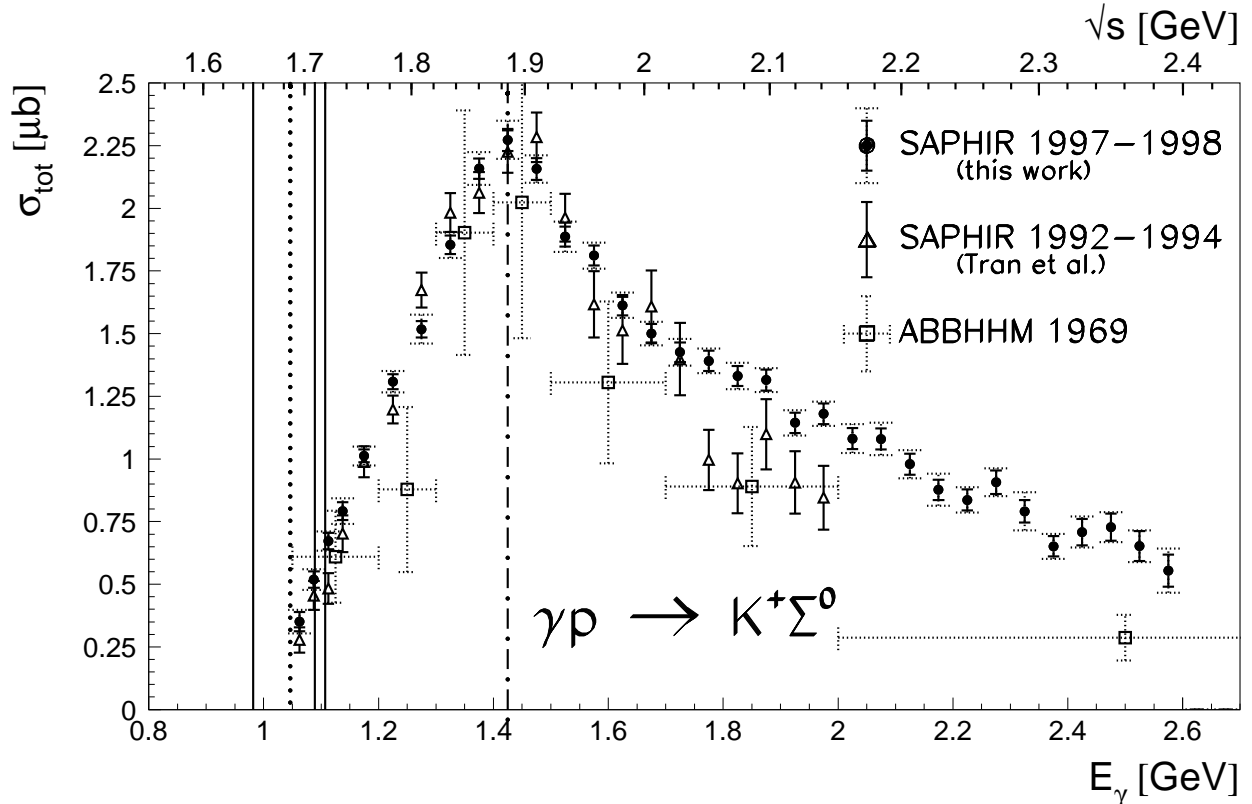


Fig. 21. Total cross section of $\gamma p \rightarrow K^+ \Sigma^0$. The vertical lines indicate the threshold energy of $\gamma p \rightarrow K^+ \Sigma^0$ (dotted) and the mass values of the known resonances $S_{11}(1650)$, $P_{11}(1710)$ and $P_{13}(1720)$ (solid). The maximum cross section (dash-dotted line) is discussed with respect to contributions of Δ -resonances at this energy region (see text).

to $\gamma p \rightarrow K^+ \Lambda$ and $\gamma p \rightarrow K^+ \Sigma^0$ give values for χ^2 between 0.4 and 1.4. For $L = 3$ the mean of χ^2 is 1.1 and 90% of the χ^2 values vary between 0.5 and 1.7. For $L = 2$ the mean is 1.3 with 90% of the χ^2 between 0.6 and 2.3. Because the fits for $L = 4$ deliver the best description over the full angular range (especially for the very forward and backward regions), $L = 4$ was used for the fits shown in Figures 12-17.

The reaction cross sections were determined as a function of energy by integrating the differential cross section over the angular range. They are shown for $\gamma p \rightarrow K^+ \Lambda$ in Fig. 20 and for $\gamma p \rightarrow K^+ \Sigma^0$ in Fig. 21.

Solid and dashed error bars were determined for the total cross sections by quadratic addition of the single errors in the angular bins of the differential cross sections per energy bin, separately for σ_w and σ_d .

For comparison, previous measurements of the total cross sections are also shown in Figures 20 and 21: the measurements of the ABBHMH collaboration [17] and the SAPHIR cross section from the first data taking periods in 1992-1994 [6] (this older SAPHIR data are not included in the current analysis).

6 Mutual event migrations of reactions

$\gamma p \rightarrow K^+ \Lambda$ and $\gamma p \rightarrow K^+ \Sigma^0$

A remaining source of background originates from the migration between $\gamma p \rightarrow K^+ \Lambda$ and $\gamma p \rightarrow K^+ \Sigma^0$ (see Fig. 3). This background was determined from Monte-Carlo generated events and was found to be on average at the level of 7% for $K^+ \Lambda$ to $K^+ \Sigma^0$ and less than 2% for $K^+ \Sigma^0$ to $K^+ \Lambda$ respectively [1]. The estimated cross sections corresponding to this background as a function of photon energy and kaon production angle are shown in Fig. 22.

All presented cross sections were corrected for this background in bins of photon energy and kaon production angle.

7 Systematic errors

The error estimates of cross sections shown in figures and tables do not include the overall systematic uncertainties which are described in the following:

- The event selection includes a cut on the probability of the kinematic fits which was set to $P(\chi^2) > 10^{-10}$. From comparing the probability distribution of experimental and simulated events after the selection it was estimated that the calculation of the cross section has an overall systematic normalization uncertainty of about 5% throughout the energy range [1] by which the true cross sections are systematically underestimated.
- Background from other reactions was estimated from Monte-Carlo generated events which passed the same reconstruction and selection criteria as the experimental events. The relative contribution from reactions

which yield non-negligible contributions to the background are shown in Table 1.

For the cross section of $\gamma p \rightarrow K^+ \Lambda$ the background reactions account for overall 5% at lower photon energies ($E_\gamma < 1.8$ GeV) and 7% at higher photon energies ($E_\gamma > 1.8$ GeV). For $\gamma p \rightarrow K^+ \Sigma^0$ the corresponding fractions are 7% and 14% respectively. This means that the true cross sections are systematically overestimated by these fractions.

The systematic shifts of cross sections caused by the two sources concern the overall normalizations. They are assumed to be independent from each other and opposite in sign so that they approximately cancel each other except for $\gamma p \rightarrow K^+ \Sigma^0$ at the higher photon energies where they combine to a 9% excess due to background events. The errors on cross sections given in figures and tables do not include these normalization errors.

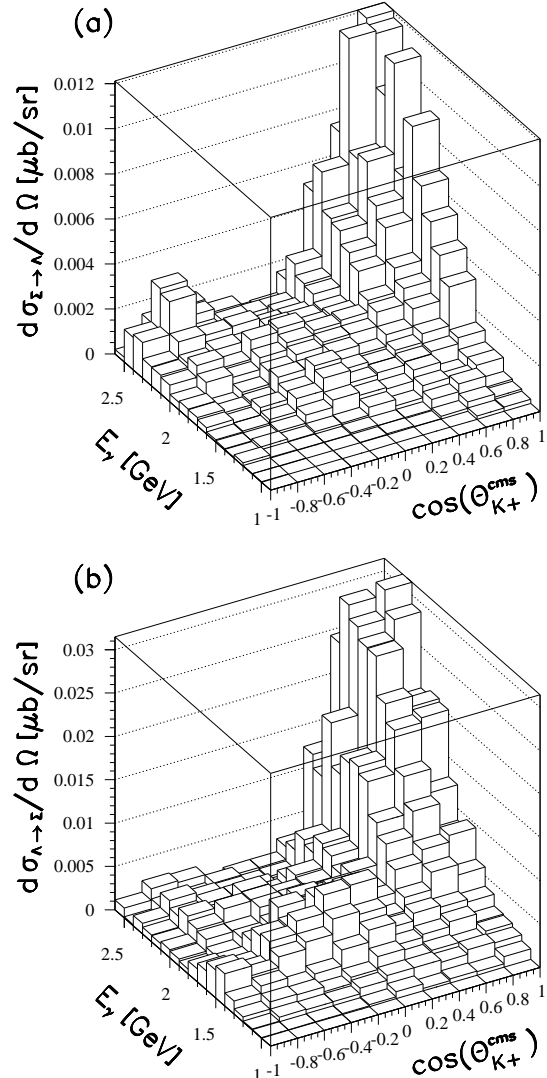


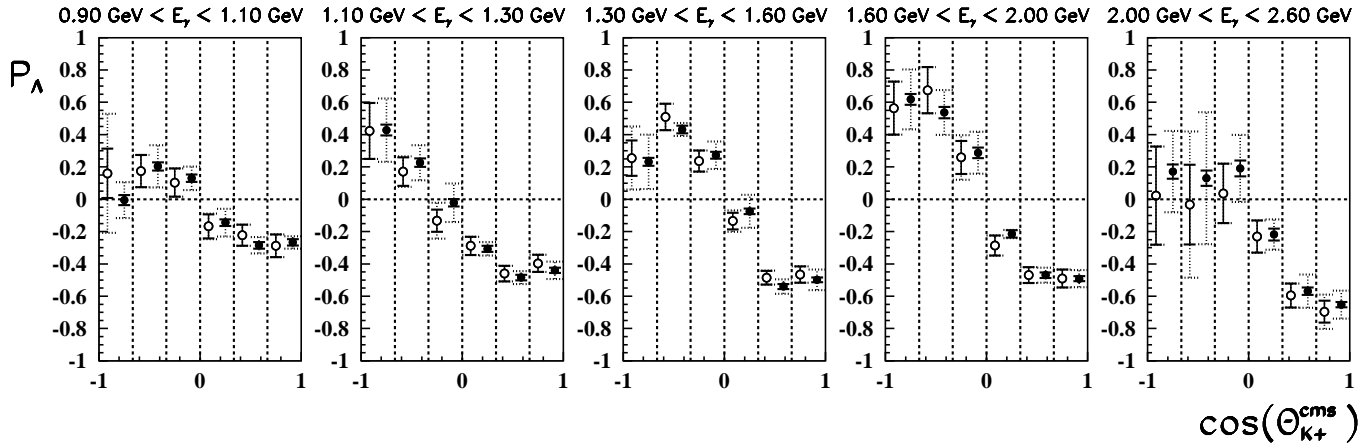
Fig. 22. Differential cross sections of background due to mutual migrations of $\gamma p \rightarrow K^+ \Lambda$ and $\gamma p \rightarrow K^+ \Sigma^0$. (a) $\gamma p \rightarrow K^+ \Sigma^0$ falsely identified as $\gamma p \rightarrow K^+ \Lambda$. (b) $\gamma p \rightarrow K^+ \Lambda$ falsely identified as $\gamma p \rightarrow K^+ \Sigma^0$.

Table 1. Background from other reactions which contribute to the cross sections of the reactions $\gamma p \rightarrow K^+ \Lambda$ and $\gamma p \rightarrow K^+ \Sigma^0$ in two energy ranges.

Background from	$\gamma p \rightarrow K^+ \Lambda$		$\gamma p \rightarrow K^+ \Sigma^0$	
	$E_\gamma < 1.8$ GeV	$E_\gamma > 1.8$ GeV	$E_\gamma < 1.8$ GeV	$E_\gamma > 1.8$ GeV
$\gamma p \rightarrow p \pi^+ \pi^-$	4.5% ($\pm 2.1\%$)	4.7% ($\pm 2.9\%$)	2.3% ($\pm 1.8\%$)	1.7% ($\pm 2.4\%$)
$\gamma p \rightarrow p \pi^+ \pi^- \pi^0$	0.4% ($\pm 0.6\%$)	2.1% ($\pm 1.5\%$)	3.0% ($\pm 1.7\%$)	10.6% ($\pm 3.3\%$)
$\gamma p \rightarrow K^+ \Lambda \pi^0$	0.0% ($\pm 0.1\%$)	0.0% ($\pm 0.1\%$)	1.1% ($\pm 1.0\%$)	1.7% ($\pm 1.3\%$)
$\gamma p \rightarrow K^0 \Lambda \pi^+$	0.0% ($\pm 0.0\%$)	0.0% ($\pm 0.0\%$)	0.3% ($\pm 0.6\%$)	0.1% ($\pm 0.3\%$)
Total	4.9% ($\pm 2.2\%$)	6.8% ($\pm 3.3\%$)	6.7% ($\pm 2.8\%$)	14.1% ($\pm 4.3\%$)

Table 2. Global systematic errors for differential and total cross sections of the reactions $\gamma p \rightarrow K^+ \Lambda$ and $\gamma p \rightarrow K^+ \Sigma^0$ in two energy ranges. A positive (negative) background value means that the calculated cross section is underestimated (overestimated) by the given fraction.

	$\gamma p \rightarrow K^+ \Lambda$		$\gamma p \rightarrow K^+ \Sigma^0$	
	$E_\gamma < 1.8$ GeV	$E_\gamma > 1.8$ GeV	$E_\gamma < 1.8$ GeV	$E_\gamma > 1.8$ GeV
Probability cut $P_{kin}(\chi^2) > 10^{-10}$	+5%	+5%	+5%	+5%
Background from $\gamma p \rightarrow p \pi^+ \pi^-$, $\gamma p \rightarrow p \pi^+ \pi^- \pi^0$ $\gamma p \rightarrow K^+ \Lambda \pi^0$ and $\gamma p \rightarrow K^0 \Lambda \pi^+$	-5%	-7%	-7%	-14%

**Fig. 23.** Λ polarizations for $\gamma p \rightarrow K^+ \Lambda$ in six bins of the kaon production angle (separated by the vertical dotted lines) and for five energy bins. The open circles are the results of fits to the angular distributions as given in the text. The full circles are results of the up-down asymmetry measurement. The two data sets are horizontally displaced for visibility.

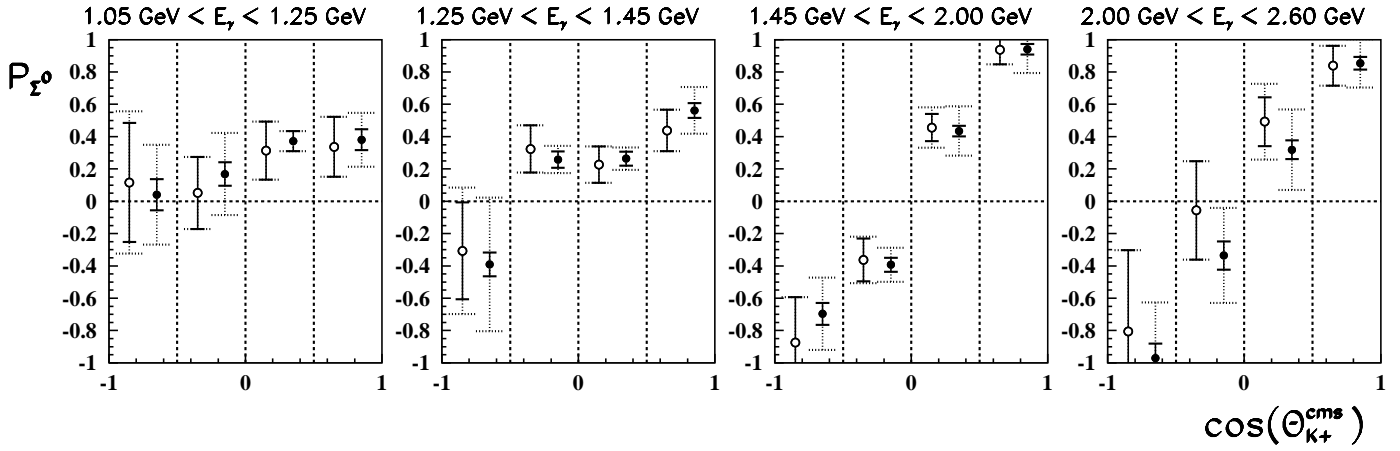


Fig. 24. Σ^0 polarizations for $\gamma p \rightarrow K^+ \Sigma^0$ in four bins of the kaon production angle (separated by the vertical dotted lines) and for four energy bins. The open circles are the results of fits to the angular distributions as given in the text. The full circles are results of the up-down asymmetry measurement. The two data sets are horizontally displaced for visual clarity.

8 Hyperon polarizations

For reactions of the type $a + b \rightarrow c + d$ with unpolarized initial state particles and conserved parity the polarization vector, \mathbf{P}_d , in the rest frame of particle d is perpendicular to the production plane [18,19], i.e. $\mathbf{P} = P \mathbf{n}$, with \mathbf{n} being normal to the production plane. Thus, for $\gamma p \rightarrow K^+ \Lambda$ and $\gamma p \rightarrow K^+ \Sigma^0$ the hyperons Λ and Σ^0 are transversely polarized, and P_Λ and P_{Σ^0} denote the polarization parameters.

The polarization of Λ in $\gamma p \rightarrow K^+ \Lambda$ can be measured by its parity violating weak decay $\Lambda \rightarrow p \pi^-$. The decay angular distribution reads [20]:

$$W(\cos \theta) d\Omega = \frac{1}{2} \left(1 + \alpha P_\Lambda \cos \theta \right) d\Omega, \quad ,$$

where $\alpha = 0.642 \pm 0.013$ [9] is the Λ decay parameter and θ is defined as the angle between the Λ decay proton and \mathbf{n} in the Λ rest frame.

For the reaction $\gamma p \rightarrow K^+ \Sigma^0$ the polarization vector of the Σ^0 is related to the polarization vector of the Λ produced in the decay $\Sigma^0 \rightarrow \Lambda \gamma$ [21]:

$$\mathbf{P}_\Lambda = - \left(\mathbf{P}_{\Sigma^0} \cdot \mathbf{u}_\Lambda \right) \mathbf{u}_\Lambda$$

where \mathbf{u}_Λ is a unit vector describing the direction of flight of the Λ in the Σ^0 rest frame. Averaging the event sample over the flight directions of Λ yields

$$\langle \mathbf{P}_\Lambda \rangle_{\mathbf{u}_\Lambda} = - \frac{1}{3} \mathbf{P}_{\Sigma^0}, \quad ,$$

i.e. it retains only 1/3 of the sensitivity to the Σ^0 polarization:

$$W(\cos \theta) d\Omega = \frac{1}{2} \left(1 - \frac{1}{3} \alpha P_{\Sigma^0} \cos \theta \right) d\Omega$$

where again θ is the proton angle in the Λ rest frame. The polarization parameters P_Λ and P_{Σ^0} have been determined by fits to the angular distributions of the decay proton in bins of kaon production angle and photon energy. In a second method P_Λ and P_{Σ^0} have been determined directly from the asymmetry of the decay angular distributions according to

$$P_\Lambda = + \frac{2}{\alpha} \frac{N_1 - N_2}{N_1 + N_2}, \quad P_{\Sigma^0} = - \frac{6}{\alpha} \frac{N_1 - N_2}{N_1 + N_2}, \quad ,$$

with N_1 and N_2 being the number of events with $\cos \theta > 0$ and $\cos \theta < 0$ respectively.

Both results are shown in Figures 23 and 24 and the values from the fits are given in Appendix B. The inner and outer error bars refer to σ_w and σ_d and were determined according to section 5.

9 Discussion of the results

The total cross section of $\gamma p \rightarrow K^+ \Lambda$ (see Fig. 20) rises steeply from threshold up to a maximum at a photon energy of about 1.1 GeV. Then, after passing a nearby flat

region around 1.45 GeV, it falls. The gross features of this shape are reflected in the fitted Legendre coefficients (see Fig. 18): The steep rise is connected with a_0 together with smaller contributions of a_1 and a_2 . The coefficient a_1 reaches a local minimum around 1.15 GeV, from where it rises to a local maximum at 1.45 GeV. Towards higher energies, a_0 falls continuously in magnitude while a_1 and a_2 vary slowly approaching non-zero values.

Calculations with effective Lagrangians [22,23,24,25] well describe previous SAPHIR data for the reaction $\gamma p \rightarrow K^+ \Lambda$ by assuming that the production of s- and p-wave resonances contributes significantly to the cross section close to threshold, while the exchange of $K^*(892)$ vector and $K_1(1270)$ pseudovector mesons in the t-channel is more important at higher energies. All model calculations relate the large s-wave contribution expressed by a_0 to the existence of the $S_{11}(1650)$ excitation and the p-wave contribution expressed by a_1 to $P_{11}(1710)$ and $P_{13}(1720)$.

The structure of the total cross section of $\gamma p \rightarrow K^+ \Lambda$ around 1.45 GeV was already observed in previous SAPHIR data [6]. Model calculations which were optimized on these data so far do not give an unambiguous picture: Including these data in their isobar model Bennhold, Mart *et al.* interpreted the broad shoulder in the total cross section at 1.45 GeV as a signal of a $D_{13}(1895)$ resonance [24,26,27,28]. Such a D_{13} resonance has been predicted within quark model calculations [2,3] in this mass range. Janssen *et al.* also found that the data description is improved by including the $D_{13}(1895)$ resonance in their effective Lagrangian approach, although they point out that also a P_{13} , P_{11} and S_{11} in the same mass region were able to describe the data [25]. Penner and Mosel who carried out a coupled channel analysis [23] obtain a fairly good description of the data without a significant contribution of a D_{13} resonance. They explain the structure in the total cross section by a non-resonant p-wave contribution, stemming from the interference between the s-channel proton and the t-channel K^* exchange. Saghai also stressed that previous $\gamma p \rightarrow K^+ \Lambda$ data can be understood without introducing new resonances [29].

In the calculations of Bennhold *et al.* an enhancement in the differential cross section for backward produced kaons in reaction $\gamma p \rightarrow K^+ \Lambda$ at 1.45 GeV due to the signal of $D_{13}(1895)$ has been predicted [27]. Such an enhancement is confirmed in the new data around the expected photon energy of 1.45 GeV as can be seen most significantly for kaon production angles in the range $-0.9 < \cos(\theta_{K^+}^{cms}) < -0.8$ (Fig. 25). A similar enhancement albeit less pronounced is also observed over the full backward hemisphere.

For $\gamma p \rightarrow K^+ \Sigma^0$ the total cross section (see Fig. 21) peaks around a photon energy of 1.45 GeV. The peak is also seen in the coefficients a_0 and a_2 (see Fig. 19). The coefficients a_1 , a_3 and a_4 change slope at a photon energy of about 1.8 GeV. With increasing energy, the contribution of a_0 becomes less important while a_1 and, on a smaller scale, also a_2 stay with non-zero contributions.

Isobar model calculations for $\gamma p \rightarrow K^+ \Sigma^0$ based on previous SAPHIR data [24,30] state that the bump at

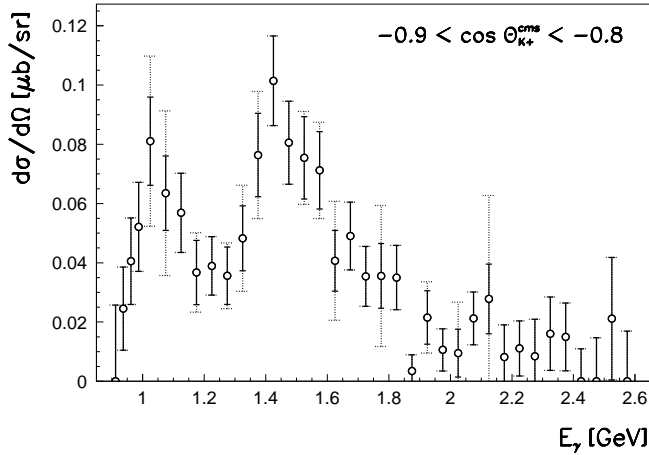


Fig. 25. The differential cross section of $\gamma p \rightarrow K^+ \Lambda$ shows an enhancement for backward produced kaons for photon energies around 1.45 GeV corresponding to a *cms* energy of 1900 MeV.

1.45 GeV could stem from the Δ resonances $S_{31}(1900)$ and $P_{31}(1910)$.

Above 2 GeV the differential cross sections of both, $\gamma p \rightarrow K^+ \Lambda$ and $\gamma p \rightarrow K^+ \Sigma^0$, show a forward peak with small contributions in the backward hemisphere only. Apparently, in this energy range the importance of s-channel resonances decreases and t-channel processes gain significance. Kaon photoproduction data for photon energies above 4 GeV are fairly well described by a model of Guidal *et al.* [31] with reggeized meson propagators. A theoretical understanding of the transition region itself is still missing and the data given here should be helpful for this issue.

Both, Λ and Σ^0 , are polarized throughout the investigated photon energy range. The following observations are made (see Figures 23 and 24):

- The polarization parameters varies strongly with the production angle of the kaon.
- They are in general opposite in sign for Λ and Σ^0 .
- The shapes of the angular dependence indicate the same signature throughout the whole energy range: it tends to be positive for Λ (negative for Σ^0) at backward angles, passes zero in the central region of $\cos(\theta_{K^+}^{cms}) \approx 0$ and shows negative (positive) values in the forward hemisphere.
- The magnitude of the polarizations parameters varies with energy, for $\gamma p \rightarrow K^+ \Lambda$ less than for $\gamma p \rightarrow K^+ \Sigma^0$. The Σ^0 is maximally polarized ($P_{\Sigma^0} = \pm 1$) at forward and backward kaon production angles for photon energies above 1.45 GeV.

The opposite signs of the angular dependence of the polarization parameters for Λ and Σ^0 are predicted from SU(6) [32] if the same production mechanism for the s-quark is assumed in both reactions.

The persistence of the shape is surprising, especially for the Λ and Σ^0 production below a photon energy of 1.3 GeV, where resonance contributions of $S_{11}(1650)$, $P_{11}(1710)$ and $P_{13}(1720)$ are found to contribute strongly. Note that the energy bin width for the polarization measurement was

chosen to be comparable to the width of the resonances. Current model calculations, which are successful to describe the cross sections in the ranges of energy and production angle for both reactions of previous data, do not describe the polarizations of Λ and Σ^0 simultaneously.

The polarizations measured for Λ and Σ^0 are similar in shape and magnitude to many other results obtained with other beams and up to highest energies [33,34], thus suggesting a general s-quark production scheme [35].

10 Summary

New measurements of the reactions $\gamma p \rightarrow K^+ \Lambda$ and $\gamma p \rightarrow K^+ \Sigma^0$ are reported. They were carried out with the SAPHIR detector at ELSA in the photon energy range from the reaction thresholds to 2.6 GeV. The results comprise cross sections and hyperon polarizations as a function of the kaon production angle and the photon energy. With respect to previous SAPHIR measurements [6], the photon energy range was extended, the differential resolution in both kaon production angle and photon energy were improved by a factor of two and errors were reduced. The cross sections indicate resonance contributions, for Λ production near threshold and for Λ and Σ^0 production around a photon energy of 1.45 GeV. The hyperons are strongly polarized. The polarizations for Λ and Σ^0 are in general opposite in sign along with a pronounced forward-backward asymmetry which varies slowly with energy.

11 Acknowledgements

We would like to thank the technical staff of the ELSA machine group for their invaluable contributions to the experiment. We gratefully acknowledge the support by the Deutsche Forschungsgemeinschaft in the framework of the Schwerpunktprogramm “Investigations of the hadronic structure of nucleons and nuclei with electromagnetic probes” (SPP 1034 KL 980/2-3).

A Differential cross sections of reactions

$\gamma p \rightarrow K^+ \Lambda$ and $\gamma p \rightarrow K^+ \Sigma^0$

The differential cross sections as function of kaon production angle and photon energy are given as $m \pm \sigma_d(\sigma_w)$. For definitions of m , σ_d and σ_w see Section 5. $m \pm \sigma_d$ should be used for theoretical calculations as σ_d accounts, in addition to statistical errors, for the spread of results obtained for the four data taking periods. It should be noted that the calculations of cross sections and errors shown in the following tables do not take into account systematic uncertainties in the overall normalization of cross sections which were estimated in section 7.

Sorry, there was not enough space for including the tables for the differential cross sections in this preprint. Ask for theses by email to glander@physik.uni-bonn.de or see the paper expected to be published soon.

Table 3. Differential cross section $\frac{d\sigma}{d\Omega}$ [$\mu\text{b}/\text{sr}$] of reaction $\gamma p \rightarrow K^+ \Lambda$ for photon energies $0.9 \text{ GeV} \leq E_\gamma \leq 1.4 \text{ GeV}$.

Table 4. Differential cross section $\frac{d\sigma}{d\Omega}$ [$\mu\text{b}/\text{sr}$] of reaction $\gamma p \rightarrow K^+ \Lambda$ for photon energies $1.4 \text{ GeV} \leq E_\gamma \leq 2.0 \text{ GeV}$.

Table 5. Differential cross section $\frac{d\sigma}{d\Omega}$ [$\mu\text{b}/\text{sr}$] of reaction $\gamma p \rightarrow K^+ \Lambda$ for photon energies $2.0 \text{ GeV} \leq E_\gamma \leq 2.6 \text{ GeV}$.

Table 6. Differential cross section $\frac{d\sigma}{d\Omega}$ [$\mu\text{b}/\text{sr}$] of reaction $\gamma p \rightarrow K^+ \Sigma^0$ for photon energies $1.05 \text{ GeV} \leq E_\gamma \leq 1.55 \text{ GeV}$.

Table 7. Differential cross section $\frac{d\sigma}{d\Omega}$ [$\mu\text{b}/\text{sr}$] of reaction $\gamma p \rightarrow K^+ \Sigma^0$ for photon energies $1.55 \text{ GeV} \leq E_\gamma \leq 2.15 \text{ GeV}$.

Table 8. Differential cross section $\frac{d\sigma}{d\Omega}$ [$\mu\text{b}/\text{sr}$] of reaction $\gamma p \rightarrow K^+ \Sigma^0$ for photon energies $2.15 \text{ GeV} \leq E_\gamma \leq 2.60 \text{ GeV}$.

B Hyperon polarizations

The polarizations are given as $m \pm \sigma_d (\sigma_w)$. For definitions of m , σ_d und σ_w see Section 5. $m \pm \sigma_d$ should be used for theoretical calculations.

Table 9. Hyperon polarization P_Λ for reaction $\gamma p \rightarrow K^+ \Lambda$ for photon energies $0.9 \text{ GeV} \leq E_\gamma \leq 2.6 \text{ GeV}$.

$\cos(\theta_{K^+}^{cms})$			$E_\gamma [\text{GeV}]$			
			0.90 - 1.10	1.10 - 1.30	1.30 - 1.60	1.60 - 2.00
-1	...	-2/3	$0.161 \pm 0.369 (0.153)$	$0.423 \pm 0.173 (0.173)$	$0.255 \pm 0.195 (0.109)$	$0.564 \pm 0.165 (0.165)$
-2/3	...	-1/3	$0.175 \pm 0.099 (0.099)$	$0.171 \pm 0.094 (0.088)$	$0.510 \pm 0.082 (0.082)$	$0.675 \pm 0.143 (0.143)$
-1/3	...	0	$0.103 \pm 0.087 (0.087)$	$-0.133 \pm 0.112 (0.069)$	$0.237 \pm 0.065 (0.065)$	$0.259 \pm 0.138 (0.103)$
0	...	1/3	$-0.168 \pm 0.079 (0.075)$	$-0.288 \pm 0.056 (0.056)$	$-0.135 \pm 0.067 (0.051)$	$-0.287 \pm 0.062 (0.062)$
1/3	...	2/3	$-0.223 \pm 0.066 (0.066)$	$-0.460 \pm 0.048 (0.048)$	$-0.485 \pm 0.043 (0.043)$	$-0.469 \pm 0.049 (0.049)$
2/3	...	1	$-0.288 \pm 0.070 (0.070)$	$-0.397 \pm 0.053 (0.053)$	$-0.466 \pm 0.051 (0.051)$	$-0.491 \pm 0.056 (0.056)$
$\cos(\theta_{K^+}^{cms})$			$E_\gamma [\text{GeV}]$			
			2.00 - 2.60			
-1	...	-2/3	$0.023 \pm 0.304 (0.304)$			
-2/3	...	-1/3	$-0.033 \pm 0.452 (0.247)$			
-1/3	...	0	$0.036 \pm 0.184 (0.184)$			
0	...	1/3	$-0.231 \pm 0.100 (0.100)$			
1/3	...	2/3	$-0.596 \pm 0.074 (0.074)$			
2/3	...	1	$-0.696 \pm 0.106 (0.068)$			

Table 10. Hyperon polarization P_{Σ^0} in reaction $\gamma p \rightarrow K^+ \Sigma^0$ for photon energies $1.05 \text{ GeV} \leq E_\gamma \leq 2.60 \text{ GeV}$.

$\cos(\theta_{K^+}^{cms})$			$E_\gamma [\text{GeV}]$			
			1.05 - 1.25	1.25 - 1.45	1.45 - 2.00	2.00 - 2.60
-1	...	-1/2	$0.116 \pm 0.440 (0.369)$	$-0.307 \pm 0.391 (0.300)$	$-0.874 \pm 0.280 (0.280)$	$-0.806 \pm 0.504 (0.504)$
-1/2	...	0	$0.052 \pm 0.223 (0.223)$	$0.324 \pm 0.146 (0.146)$	$-0.363 \pm 0.143 (0.132)$	$-0.057 \pm 0.304 (0.304)$
0	...	1/2	$0.313 \pm 0.180 (0.180)$	$0.226 \pm 0.113 (0.113)$	$0.456 \pm 0.125 (0.084)$	$0.493 \pm 0.234 (0.151)$
1/2	...	1	$0.336 \pm 0.185 (0.185)$	$0.438 \pm 0.128 (0.128)$	$0.937 \pm 0.089 (0.089)$	$0.839 \pm 0.123 (0.123)$

References

1. K.-H. Glander: doctoral thesis Bonn 2003, BONN-IR-2003-05; to be found on the web:
<http://saphir.physik.uni-bonn.de/saphir/thesis.html>
2. S. Capstick, W. Roberts: Phys. Rev. D **58**, 074011 (1998)
3. U. Löring, B. Ch. Metsch, H. R. Petry: Eur. Phys. J. A **10**, 395 (2001)
4. W. J. Schuille *et al.*: Nucl. Instr. Meth. A **344**, 470 (1994)
5. D. Husmann, W. J. Schuille: Phys. Bl. **44**, 40 (1988)
6. M. Q. Tran *et al.*: Phys. Lett. B **445**, 20 (1998)
7. R. Burgwinkel: doctoral thesis Bonn 1996, Bonn IR-96-02
8. J. Barth: doctoral thesis Bonn 2002, BONN-IR-02-6
9. Particle Data Group (K. Hagiwara *et al.*): Phys. Rev. D **66**, 010001 (2002)
10. R. Brun, F. Carena *et al.*: GEANT Simulating Program for Particle Physics Experiments, Version 2.0, CERN DD/US/86
11. J. Barth *et al.*: Low-energy photoproduction of ω -mesons, accepted for publication in Eur. Phys. J.
12. J. Hannappel: doctoral thesis Bonn 1997, BONN-IR-97-15
13. W. Neuberburg: doctoral thesis Bonn 1999, BONN-IR-99-06
14. Landolt-Börnstein: Numerical Data and Functional Relationships in Science and Technology, New Series I/12b (1988)
15. J. Barth *et al.*: Low-energy photoproduction of Φ -mesons, Eur. Phys. J. A **17**, 269-274 (2003)
16. C. Wu *et al.*: ρ photoproduction at SAPHIR, in preparation
17. ABBHHM collaboration: Phys. Rev. **188**, 2060 (1969)
18. M. Jacob, G. C. Wick: Annals of Physics **7**, 404 (1959)
19. K. Gottfried, J. D. Jackson: Nuovo Cimento **33**, 309 (1964)
20. T. D. Lee, C. N. Yang: Phys. Rev. **108**, 1645 (1957)
21. R. Gatto: Phys. Rev. **109**, 610 (1958)
22. T. Feuster and U. Mosel: Phys. Rev. C **59**, 460 (1999)
23. G. Penner and U. Mosel: Phys. Rev. C **66**, 055212 (2002)
24. C. Bennhold, T. Mart, A. Waluyo, H. Haberzettl, G. Penner, T. Feuster, U. Mosel: *Preprint* nucl-th/9901066
25. S. Janssen, J. Ryckebusch, W. Van Nespen, D. Debruyne, T. Van Cauteren: Eur. Phys. J. A **11**, 105 (2001)
26. T. Mart and C. Bennhold: Phys. Rev. C **61**, (R)012201 (2000)
27. C. Bennhold, H. Haberzettl, T. Mart: *Proceedings of the Second International Conference on Perspectives in Hadronic Physics*, edited by Sigfrido Boffi, Claudio Ciofi degli Atti & Mauro Giannini (World Scientific, 1999)
28. C. Bennhold, A. Waluyo, H. Haberzettl, T. Mart, G. Penner, U. Mosel: *Preprint* nucl-th/0008024
29. B. Saghai: *Preprint* nucl-th/0105001
30. S. Janssen, J. Ryckebusch, D. Debruyne, T. Van Cauteren: Phys. Rev. C **66**, 035202 (2002)
31. M. Guidal, J.-M. Laget, M. Vanderhaeghen: Nucl. Phys. A **627**, 645 (1997);
32. See e.g. W. Thirring: Acta Physica Austriaca **Sup. II** (1966)
33. E. Paul: Italian Phys. Society 1992, Vol. 44, Proc. of the Conference on THE ELFE PROJECT, Mainz 1992, p. 379
34. K. Heller: Proc. of the 9th International Symposium on High Energy Spin Physics, Bonn 1990, Springer ISBN 3-540-54127-6
35. Th. A. DeGrand and H. Miettinen: Phys. Rev. D **24**, 2419 (1981)